Experimental study and hybrid correlation-residual neural network modeling of pressure gradient for two-phase refrigerant flowing in small tubes

Houpei Li [a,b,*] , Lei Wang [a,b], Wenzhe Li [c]

[a] *College of Civil Engineering, Hunan University, Changsha, 410082, China*
[b] *Key Laboratory of Building Safety and Energy Efficiency (Hunan University), Ministry of Education, China*
[c] *School of Energy Science and Engineering, Central South University, Changsha, 410083, China*

ARTICLE INFO

ABSTRACT

Accurate prediction of two-phase pressure gradient (dP/dz) in small-diameter tubes is critical for the reliable design and optimization of advanced thermal systems. Conventional empirical and mechanistic correlations often fail to capture the complex, nonlinear behaviors of two-phase flow, leading to significant uncertainties. In this study, a Hybrid Correlation–Residual Neural Network (C-RNN) modeling framework is developed and validated for predicting the two-phase frictional dP/dz in horizontal tubes with inner diameters of 1–3 mm. The experimental investigation involves five refrigerants: R1234yf, R134a, R1234ze(E), R1233zd(E), and R32, and the test conditions cover mass fluxes from 100 to 300 kg m^{-2}s^{-1} and saturation temperatures from 5 to 25 °C. The hybrid modeling approach first applies a well-established physical correlation (base model) to obtain a baseline prediction for dP/dz, then employs a feed-forward Artificial Neural Network (ANN) to correct the residual as a function of key nondimensional numbers. The effect of base models, input layers, hidden layer structures on accuracy and trainable parameters are tested. This methodology retains physical interpretability while capturing the complex, data-driven dependencies and systematic deviations observed in experiments. Results demonstrate that the proposed C-RNN model achieves excellent agreement with experimental measurements across all tested refrigerants and conditions. The mean percentage absolute error (MPAE) is reduced to below 6 % (classical correlations are 15–24 %).

1. Introduction

Accurate prediction of two-phase pressure gradients of two-phase flow is important for the design of modern thermal system such as refrigerators, air conditioning units, heat exchangers, electronic cooling devices, etc. [1]. In these applications, pressure drop directly impacts pumping or compressing power and system efficiency [2]. Therefore, understanding the pressure gradient and accurately estimating the pressure drop become more and more essential. Resent years, compact heat exchangers become more and more attractive for their high surface area to volume ratio [3]. On one hand, the microchannel heat exchangers usually use small tube with the hydraulic diameter at the scale of 1 mm. On the other hand, as the outer diameter of the fin-tube heat exchanger reduces from ~7 to ~5 mm, the inner diameter is also reduced from ~5 to ~3 mm. The pressure drop estimation of these small

tube heat exchanger is not only important for designing and sizing, but also significant for flow rate balancing and maldistribution [4]. Consequently, reliable pressure drop prediction for small tubes are of high importance in optimizing such systems [5].

Another key driving factor for improving pressure gradient understanding and modeling is the transition to low-GWP refrigerants [6]. Hydrofluorocarbons such as R134a are being phased out due to environmental concerns, while alternatives like R1234yf and R1234ze(E) provide lower GWP with similar thermodynamic properties [7,8]. For example, R1234yf shows comparable properties to R134a and is already widely adopted, although studies report slightly lower cooling capacity [9]. R32, with higher latent heat, offers greater cooling capacity but exhibits higher discharge pressure and flammability issues [10]. R1234ze(E) demonstrates favorable performance in low-temperature heat pumps [11], while R1233zd(E) is considered a promising substitute for R245fa in organic Rankine cycles due to its similar heat transfer

---

* Corresponding author.
E-mail address: houpei@hnu.edu.cn (H. Li).

Nomenclature

Abbreviations and variables

ANN	Artificial Neural Network (/)
Bo	Bond number (-)
CFD	Computational Fluid Dynamics (/)
Cor	Correlation coefficient (-)
C-RNN	Correlation-Residual Neural Network (/)
D	diameter (mm)
DP	Differential pressure (kPa)
$\frac{dP}{dz}$	Pressure gradient (kPa m^{-1})
Fr	Froude number (-)
Func	Functional relationship (/)
G	Mass flux (kg-m^{-2}s^{-1})
GWP	Global Warming Potential (-)
h	Specific enthalpy (kJ-kg^{-1})
L	Length (mm)
MPE	Mean percentage error (-)
MPAE	Mean percentage absolute error (-)
MSE	Mean squared Error (-)
$\dot{m}$	Mass flow rate (kg-s^{-1})
P	Pressure (kPa)
PINN	Physics-Informed Neural Network (/)
PD	Pressure drop (kPa)
Q	Heat transfer rate (kW)
RTD	Resistance thermometer (/)
Re	Reynolds number (-)

R	Residual (-)
ReLU	Rectified Linear Unit (/)
std	Standard deviation (-)
T	Temperature (°C)
var	variables (/)
We	Weber number (-)
X	Lockhart-Martinelli parameter (-)
x	Vapor quality (-)

Greek letters

μ	Dynamic viscosity (kg-m^{-1}s^{-1})
ρ	Density (kg-m^{-3})
σ	Surface tension (N-m^{-1})

Subscripts

i	Index
in	Inlet
ins	instrumental
l	Liquid
lo	Only liquid
ph	preheater
R	reduced
sat	Saturation
ts	Testing section
v	Vapor
vo	Only vapor
var	Variables

behavior [12].

These low-GWP alternative refrigerants are of high interest in both the academic and engineering fields. Their flowing characteristics are also studied by many researchers under a variety of geometries and working fluids. A review study by Fazelnia et al. [13] supports adoption of R1234yf as a sustainable alternative to R134a, addressing regulatory needs. They conclude that the main flow regime of R1234yf in horizontal circular tubes are mainly slug-stratified wavy, stratified wavy, slug-intermittent, and annular flow. Pressure gradient of R1234yf increases with both mass flux and vapor quality. Garcia Pabon et al. [14] experimentally investigate the two-phase pressure gradient of R1234yf in horizontal smooth tubes (3.2–8.0 mm diameter) under varying conditions. They find that R1234yf exhibited about 20 % lower pressure gradient than R134a, attributed to its lower liquid viscosity and higher vapor density. Pressure gradient of R1234yf increases with mass velocity and decreases with tube diameter and saturation temperature. They report that the peak pressure gradients occurred at vapor qualities of 0.75–0.95. Li and Hrnjak [15] report that pressure gradient of R1234yf rises with vapor quality and mass flux, while higher saturation temperatures reduced gradients. They also study the pressure gradient of R134a and showing a similar trend [16]. Arcasi et al. [17] investigate the adiabatic frictional pressure gradient during flow boiling of pure refrigerant R1233zd in a horizontal stainless-steel tube (6 mm diameter). They show that the frictional pressure gradient peaks at intermediate vapor qualities, increasing with mass flux but decreasing with higher saturation temperatures due to reduced vapor-to-liquid density ratios. Huang et al. [18] explore flow boiling pressure gradient of R1233zd(E) in a multi-microchannel evaporator (67 channels) and proposes a new empirical pressure gradient model for high mass fluxes. Ramírez-Rivera et al. [19] experimentally investigate two-phase flow pressure drop during evaporation and condensation of refrigerants R134a and R32 in multiport mini-channel tubes. They show that pressure gradient increases with mass flux and vapor quality but decreases with higher saturation temperatures due to reduced density ratios. R134a exhibits higher pressure gradient than R32, attributed to its lower

reduced pressure and higher liquid-vapor density ratios. Righetti et al. [20] study R1233zd(E) flow boiling inside a 4.3 mm micro-fin tube. They show that the two-phase pressure gradient increases with both mass flux and vapor quality. These findings of R1233zd(E) are similar to Huang et al. [18]. Comparing among studies [16,21,22], it can be found that as the tube diameter is smaller, the pressure gradient is higher.

In general, as tube diameter shrinks, the pressure gradient increases. The mass flux, vapor quality, and saturation temperature all have notable effects on pressure gradient. In addition, two-phase flow pressure gradient has traditionally been addressed with empirical correlations and mechanistic models. One of the ideas to predict two-phase pressure gradient is to use two-phase parameters in a single-phase predictive correlation, and this kind of model is called a homogeneous model. The first widely used homogeneous model for refrigerants was proposed by Cicchitti et al. [23]. The other classical examples include McAdams [24], Dukler et al. [25], and Beattie and Whalley [26]. They express the two-phase frictional gradient by assuming velocity and thermal equilibrium between phases. More recently, Tibiriçá et al. [27] develop a complete set of optimized homogeneous correlations for microchannel flow boiling and two-phase flow, achieving improved accuracy. Lockhart and Martinelli [28] pioneers a separated-flow approach, introducing the concept of a two-phase friction multiplier to scale single-phase pressure losses. Building on this foundation, many correlations have been proposed to fit experimental data in specific regime, for example, the Friedel correlation [29] and the Chisholm correlation [30] are well-known for frictional pressure gradient in horizontal flows. These classical correlations, often based on dimensional analysis and curve-fitting, can work adequately in the ranges for which they were developed, but their accuracy tends to deteriorate when extrapolated to new fluids or geometries. Recognizing the shortcomings of applying macroscale models to microscale channels, researchers have developed specialized mini/micro-channel correlations. Mishima and Hibiki [31] introduces a modified two-phase multiplier that explicitly accounts for tube diameter effects in small tubes. Kim and Mudawar [32] presents a universal correlation intended for mini/micro-channel

flows. While these tailored models improve upon classical ones, they still often show limited generality. Sun and Mishima [33] compares dozens of existing methods against an ensemble of mini-channel data and found large discrepancies. They conclude that no single correlation could reliably predict all data sets, with errors frequently exceeding 30 %. However, those correlations based on macroscale experimental results can also succeed in microchannel tubes. For example, several studies [17,34] show the accuracy of adopting Müller-Steinhagen and Heck [35] in microchannel tube. Another approach is to analysis the flow pattern based on basic fluid dynamic and heat transfer equations. Li and Hrnjak [36] proposes a new mechanistic model based on annular flow in small tubes, and the model predict heat transfer coefficients, pressure gradients, and void fraction simultaneously. Their model adopted the flow pattern analysis from Field and Hrnjak [37]. Similar flow pattern analysis can be found in Thome et al. [38] which is built for condensation heat transfer coefficient prediction. The two-zone [39] and three-zone [40] model are also proposed for predicting the two-phase flow characteristics in small tubes. A recent contribution is the model of Mauro et al. [41], who propose a mechanistic predictive method for pressure drop and void fraction in annular flows with improved fidelity under microchannel conditions. These models predict heat transfer coefficient based on calculating the important flow pattern geometry such as liquid film thickness. In the meantime, an empirical or analytical formular for the interfacial frictional factor combined with the single-phase frictional factor can be adopted for predicting pressure gradients.

Machine Learning methods offer a flexible way to approximate complex non-linear relationships in multiphase flows. Li et al. [42] collect 415 experimental data points for air-water two-phase flow in inclined pipeline-riser systems and trained an Artificial Neural Network using superficial gas and liquid velocities and riser inclination as inputs. A network with a single hidden layer and 14 neurons achieved a Mean Percent Absolute Error (MPAE) of 3.35 % and an R^2 of 0.995 when predicting pressure gradient. These results illustrate that even simple feed-forward neural networks can provide highly accurate predictions when trained on well curated data. Multiple hidden layers may improve the prediction accuracy, for example, Li et al. [43] tests the ANN model with 6–10 hidden layers for pressure gradient prediction. They achieve a low MPAE (8.3 %). They suggest that when building the predictive ANN, it is important to compare different combinations of nondimensional numbers as input layer, and the structure of hidden layers, and it is very important to the prediction accuracy. Another predictive study with Committee Neural Network obtains a mean error of 5.79 % [44]. Khosravi et al. [45] train multilayer feed-forward neural networks, support-vector regression, and other types of machine learning networks for testing the behavior. They highlight that compact ML models can capture frictional dP/dz trends with high fidelity under controlled ranges, but also highlight the limited coverage of single-fluid datasets. Chen et al. [46] assemble an evaporating-flow database of 1954 pressure drop points across seven refrigerants (R1234yf, R1234ze(E), R134a, R22, R410A, R744, R717) spanning hydraulic diameters from 0.509 to 14 mm. More recently, Mauro et al. [47] further assess a database of ~8000 points and trained shallow ANNs with varying inputs and outputs. Their best work achieve a low MAPE of 16.8 %. Importantly, they also caution that ANN may not preserve physical monotonicity or trend, underscoring the need to embed physics in ML predictors. These similar ANN based modeling approaches are also found in two-phase heat transfer coefficient studies [48,49]. While promising, neural networks trained purely on data may extrapolate poorly outside the training domain and offer limited physical insight. A more recent development is the Physics-Informed Neural Network (PINN), which incorporates governing equations as soft constraints in the loss function. Buhendwa et al. [50] used PINNs to solve forward and inverse two-phase flow problems, inferring continuous velocity and pressure fields from interface motion data and demonstrating that appropriate weighting of the residuals of the governing equations is crucial for accurate predictions. By

leveraging both data and physics, PINNs offer a path toward machine-learning models that remain anchored in the underlying fundamentals. Similar PINN technique combined with Computational Fluid Dynamics (CFD) is developed by Jalili et al. [51], and the prediction accuracy is significantly improved for predicting film boiling heat transfer. The pure ANN studies may lack physics support, but the PINN combined with CFD still has high training and computing cost compared to the ANN models. Montanez-Barrera et al. [52] proposes a new method to model pressure gradient in microchannels with both an empirical correlation and an ANN model. This new model leverages both the generalizability, capturing of fundamental fluid dynamic principles, and refines prediction to conquer the limitations of correlations in specific scenarios. Passarelli et al. [53] also compare CINN with and traditional ANN and correlations. The CINN shows slightly lower raw accuracy, but it exhibits superior reliability and physical consistency. This hybrid approach bridges the gap between purely empirical correlations (limited accuracy) and pure data-driven models (limited generalizability).

Inspired by the CINN proposed by Montanez-Barrera et al. [52], this study uses the prediction from correlation as a base, and the residual (error) is corrected by an ANN model. Thus, this new proposed model is different to the previous study [52] which uses the calculated pressure gradient, vapor quality, and internal diameter as input layer. In this study, the input parameters of ANN as well as the structure of hidden layer are tested. Another motivation of this study is to comprehensively report the hydraulic behavior (pressure gradient) for two-phase refrigerant in small tubes.

In this study, a new Hybrid Correlation-Residual Neural Network (C-RNN) model for predicting two-phase frictional pressure gradients in small horizontal tubes is built. The study begins with an extensive experimental campaign measuring flow boiling pressure drops of five refrigerants (R1234yf, R134a, R1234ze(E), R1233zd(E), and R32) in smooth copper round tubes of 1–3 mm inner diameter. These fluids span a wide range of fluid properties (molecular weights, vapor densities, surface tensions), including both legacy and new low GWP refrigerants, ensuring a broad applicability of the findings. Using the measurements as a database, a new hybrid C-RNN modeling framework is proposed. In this framework, a chosen empirical correlation provides an initial prediction of the two-phase pressure gradient, and a feed-forward neural network predicts the residual (the difference between correlation output and true value) as a function of key flow parameters. The hybrid model thus retains the physical interpretability and baseline accuracy of a correlation while employing machine learning to account for complex, non-linear deviations. The ultimate goal of proposing this framework is to enhance predictive accuracy for two-phase pressure drops across a wide spectrum of refrigerants and flow conditions, thereby improving confidence in the design of compact two-phase thermal systems.

2. Experimental preparation

2.1. Facility description

Fig. 1 presents the schematic of the experimental facility for this investigation of pressure gradient during two-phase refrigerants flowing in small diameter tubes. With the primary test section comprising smooth and horizontal copper tubes of 1, 2, and 3 mm in inner diameter. The facility was originally described in [54] and subsequently modified to enhance the accuracy of pressure drop measurements. A precision gear pump is powered by a stepper motor. The pump delivers the refrigerant flow. Mass flow rate is measured using a Coriolis-type flowmeter positions at the downstream of a 500 mm straight inlet tube, which ensures stabilized flow conditions upstream of the measurement point. Refrigerant is previously stored in a fluid tank reservoir connected to a temperature-controlled thermal bath, enabling stable control of saturation temperature and pressure, as well as facilitating reliable charge management within the main circulation loop.

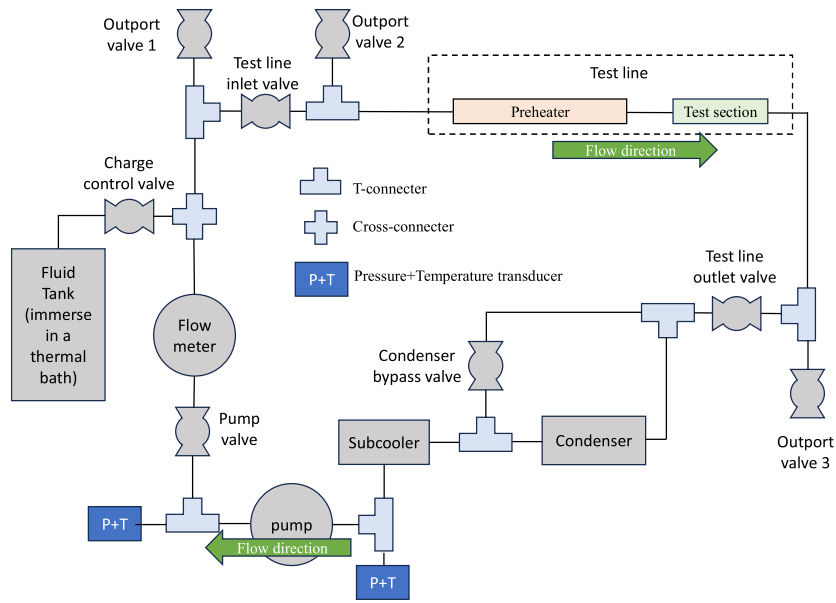Upstream of the pump, two plate heat exchangers are used for

Fig. 1. Schematic of the facility.

condensation and subcooling of the refrigerant. Subcooling is verified by pressure-temperature measurements at the pump inlet and outlet to protect the pump and avoid vapor occurrence in the pump.

2.2. Measurement setting

The experimental test line is shown in Fig. 2. The test line includes a preheater and the test section. The preheater adjusts the inlet thermodynamic state to achieve the desired vapor quality entering the test section. Absolute and differential pressure transducers (3051 s type) are installed at the test section inlet and across the section to accurately determine local pressure and pressure drop. Two class 1/3B PT100 thermometers are installed in direct contact with the refrigerants in order to provide measurements of fluid temperature for thermodynamic state determination. The test sections are 150 mm long, and the inner diameters are 1, 2, and 3 mm. All connectors in the flow path are internally matched to the test tube diameter to minimize entrance and exit disturbances to the flow. In this way, the measurement accuracy is ensured. Another design to ensure the accuracy is the dual-transducer design. Two pressure transducers are installed at the same location in parallel. These two transducers have two different ranges. When the measurement beyond the sensor with smaller range, the reading from the sensor with larger range is used. So, the uncertainty of measuring pressure and pressure drop can be further minimized.

Measurement signals from all transducers are digitized using a 24-bit data logger (4–20 mA input). Refrigerant temperatures were monitored using a dedicated module optimized for resistance thermometer (RTD) sensors. A custom LabVIEW-based code synchronized acquisition of pressure, temperature, mass flow rate, and electrical signals via RS485 communication.

2.3. Data reduction and uncertainty analysis

The local pressure gradient, dP/dz, is calculated as the pressure drop (PD) across the test section divided by its measured length (L, 150 mm).

$$dP/dz = PD/L \tag{1}$$

The saturation pressure and fluid thermodynamic properties are obtained using measured pressures and temperatures as input to REFPROP [55]. The vapor quality at the test section inlet and outlet is calculated by enthalpy balance, based on measured flow rates, preheater energy input, and refrigerant properties.

$$x = f(P_{sat}, \ h_{ts}) \tag{2}$$

The specific enthalpy is determined using the thermal equilibrium equation. For example, the specific enthalpy at inlet of the test section (same as the outlet of the preheater, $h_{ts,in}$) is determined using the specific enthalpy at the inlet of preheater ($h_{ph,in}$), heat added to the preheater (Q_{ph}), and the mass flow rate of the refrigerant ($\dot{m}$). The specific enthalpy at the inlet of preheater can be determined by the measured
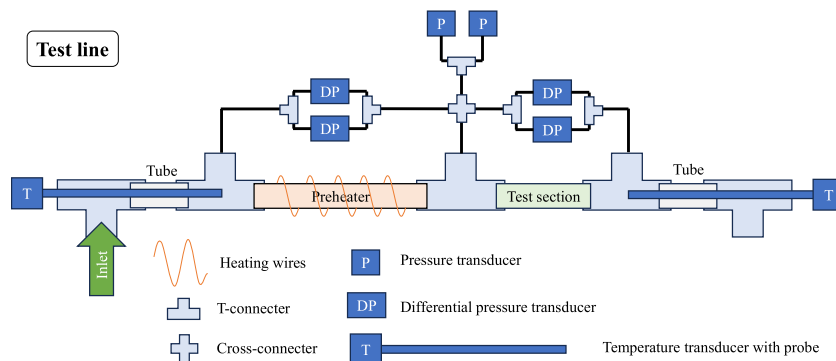

Fig. 2. Illustration of a test setup.

pressure and temperature since the refrigerant is at subcooled state. The outlet and averaged specific enthalpy of the test section can be determined using the same approach. The heat transferred from the preheater to the refrigerant side (Q_{ph}) is calibrated for its heat losses.

$$h_{ts,in} = h_{ph,in} + \frac{Q_{ph}}{\dot{m}} \tag{3}$$

The inlet pressure of the test section (P_{in}) and the pressure drop across the tube (DP_{ts}) are measured, and the saturation pressure can be then calculated.

$$P_{sat} = P_{ts,in} - DP_{ts}/2 \tag{4}$$

The estimation of saturation pressure assumed a linear pressure gradient in the test section, which was valid for small vapor quality change. During the measurement of the pressure gradient, the vapor quality change is as small as possible, so this assumption holds.

Experimental uncertainty is assessed following standard propagation methods [56]. Each variable's combined standard uncertainty is computed from both instrumental specifications and the standard deviation of repeated measurements, assuming normal statistical distribution and independence.

The combined standard uncertainty for a result (μ_{Result}), which is a function of several independent variables (var_i):

$$\mu_{Result} = \sqrt{\sum_{i=1}^{n} \left(\mu_{var_i} \frac{\partial Func}{\partial var_i} \right)^2} \tag{5}$$

Here, μ_{Result} was the total uncertainty of the result, $Func$ was the functional relationship between variables (var_i) and result, and μ_{var_i} represented the uncertainty associated with each variable var_i.

Each variable uncertainty μ_{var} is determined by both the instrumental (systematic) uncertainty ($\mu_{var,\,ins}$) and the standard deviation of the repeated measurements (std_{var}):

$$\mu_{var} = \sqrt{\left(\mu_{var,\,ins} \right)^2 + \left(std_{var} \right)^2} \tag{6}$$

At least 120 data points are recorded for each steady-state operating condition. The uncertainties for all principal measurement parameters are summarized in Table 1. All critical instruments are either factory calibrated, or lab calibrated prior to use. The derived uncertainties of vapor quality (x) and pressure gradient (dP/dz) are listed in Table 2.

A summary of measured and derived uncertainties is presented in

Table 1
Uncertainties of instruments.

Parameters	Instrument	Instrumental uncertainties	Standard deviation of measurements
Absolute pressure	3051s pressure transducer	0.075 % of the scale	0.126 to 0.689 kPa
Differential pressure	3051s pressure transducer	0.075 % of the scale	0.0071 to 0.273 kPa
Wall temperature	T Type thermocouple (after calibration)	0.12 to 0.18 °C	0.0050 to 0.0757 °C
Refrigerant temperature	Class 1/3B PT100 thermometer	0.10 °C	0.0069 to 0.0378 °C
Refrigerant mass flow rate	Coriolis-type flowmeter	0.10 %	0.00037–0.00801 g-s^{-1}
Heating power	Direct-Current power meter	0.1 % of reading + 0.05 % of scale + 0.01 mV, 0.1 % of reading + 0.05 % of scale + 0.01mA	<0.001 V, <0.001 A
Length	Digital dial caliper	0.01 mm	n.d.
Diameter	Digital microscope	0.0077 mm (130 pixels per mm)	n.d.

Table 2
Calculated uncertainties of derived parameters.

Derived parameters	Range	Uncertainties
Vapor quality (x)	0.0033~1.00	0.00132~0.00476
Pressure gradient (dP/dz)	0.05794~120.6 kPa m^{-1}	0.0400~0.297 kPa m^{-1}

Table 2.

The propagated uncertainty of the pressure gradient measurement was found to range from 0.04 to 0.297 kPa m^{-1}, depending on operating conditions. As the measured gradients reached values up to ~120 kPa m^{-1}, this corresponds to a relative uncertainty typically below 1 %.

2.4. Single-phase validation

Single-phase flow validation was conducted using R1234yf, confirming the accuracy of the pressure gradient measurements by comparison with published and widely-accepted correlation (Churchill [57]). The validation results are presented in Fig. 3. The single-phase pressure gradient is always within 8 % of the prediction from Churchill's equations except for $1600 < Re < 3000$. It seems that the transition occurs when the Reynolds number is larger than 1600 and less than 3000. In the transitional region, the discrepancy between the measurement and the prediction is 12.0~21.2 %.

3. The database

3.1. Test conditions

Table 3 summarizes the matrix of test conditions explored in this study. Experiments are conducted using a range of refrigerants, including R1234yf, R134a, R1234ze(E), and R32 from 5 to 25 °C, with additional measurements for R1233zd(E) at 25 °C only. The mass flux varies from 100 to 300 kg-m^{-2}s^{-1} to cover both low and moderate flow regimes relevant to microchannel and compact heat exchanger applications. The saturation temperature is controlled within the range of 5 to 25 °C to provide variation in thermophysical properties. Vapor quality spans from 0 (subcooled liquid) to 1 (saturated vapor) to characterize the entire two-phase flow regime. The internal diameter of test sections are 1, 2, and 3 mm in order to investigate the small-diameter effects on pressure gradient behavior across multiple refrigerants and flow conditions.

3.2. Summary of the database

The distributions of thermophysical properties and non-dimensional numbers are plotted as box plot to represent the minimum, maximum, 25 % quartile, 75 % quartile, median (box central line), and mean values
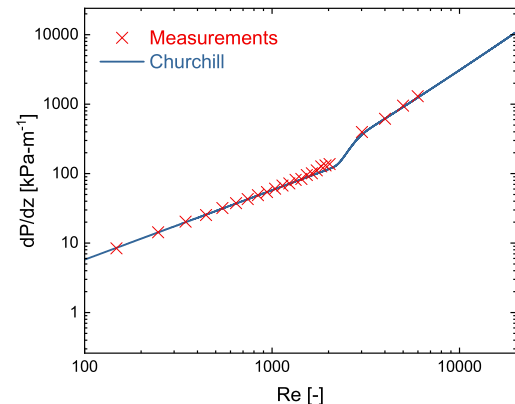
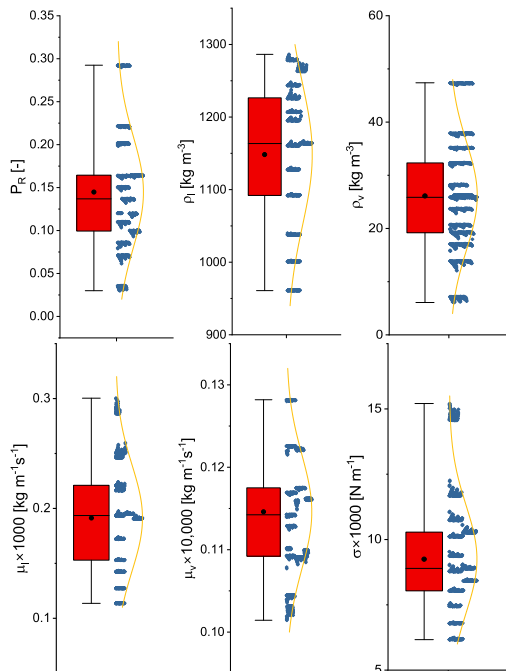**Fig. 3.** Single-phase validation of R1234yf pressure gradient.

Table 3
Test conditions.

Refrigerant	T_{sat} (°C)	Mass flux (kg·m^{-2}s^{-1})	Vapor quality (-)	Total datapoints
R1234yf	5–25	100–300	0–1	286
R134a	5–25	100–300	0–1	357
R1234ze(E)	5–25	100–300	0–1	346
R32	5–25	100–300	0–1	326
R1233zd (E)	25	100–300	0–1	110

(black scatter). Also, the values are plotted, and a distribution curve is drawn along with the box plot. The comprehensive spread of thermophysical and non-dimensional parameters captured in this dataset is essential for concluding the two-phase pressure gradient investigation and developing a robust predictive model.

Fig. 4 shows the distribution of six thermophysical properties, including reduced pressure (P_R), liquid and vapor densities (ρ_l, ρ_v), liquid and vapor viscosities (μ_l, μ_v), and surface tension (σ). These statistics provide an overview of the range and central tendency of property values sampled by the database. This information ensures the generality and robustness of the developed pressure gradient model in the later section.

The reduced pressure (P_R) is defined as the ratio of system pressure to the critical pressure. It has a mean value of 0.145, and it ranges from 0.030 to 0.292. This distribution covers typical operational regimes for low- and medium-pressure refrigerants under saturated conditions. The interquartile range (25 % to 75 % quartile) varies from 0.099 to 0.164. Liquid density (ρ_l) shows a mean of 1148 kg m^{-3}, with a minimum of 961 kg m^{-3}, and a maximum of 1286 kg m^{-3}. The 25th and 75th percentiles are 1092 and 1227 kg m^{-3}, respectively, reflecting the temperature dependence and refrigerant selection across test conditions. Vapor density (ρ_v) varies much more widely, with a mean of 26.1 kg m^{-3}, a minimum of 6.1 kg m^{-3}, and a maximum of 47.4 kg m^{-3}. For viscosity, the liquid phase (μ_l) has a mean value of 0.191 mPas (0.191×10^{-3} kg m^{-1}s^{-1}), with the central half of the data ranging from 0.153 to 0.221 mPas. The vapor viscosity (μ_v) is an order of magnitude lower, averaging 1.15×10^{-5} Pas (0.115×10^{-5} kg m^{-1}s^{-1}), with relatively narrow spread from

1.01 to 1.28×10^{-5} Pas. Surface tension (σ) averages 9.25 mN m^{-1}, with a minimum of 6.17 and a maximum of 15.2 mN m^{-1}. The variation in properties is obtained by changing the fluid saturation temperature and fluid type during the experiments.

Fig. 5 shows the distribution of calculated non-dimensional numbers of the database. They are:

- Reynolds number (Re_l, Re_v, Re_{lo}, Re_{vo}. subscripts l, v: liquid, vapor; lo, vo: assuming the tube is filled with only liquid or vapor, respectively)
- Weber number (We_l, We_v, We_{lo}, We_{vo})
- Froude number (Fr_l, Fr_v, Fr_{lo}, Fr_{vo})
- Bond number (Bo)
- X parameter (Lockhart-Martinelli)
- Density ratio (ρ_l/ρ_v)
- Viscosity ratio (μ_l/μ_v)

The liquid-phase Reynolds number (Re_l) covers a wide range, with a minimal around 0.37 and a max above 1500, spanning laminar to transitional regimes. Vapor-phase Reynolds number (Re_v) is much higher (min~10, mean ~18,000, max ~25,000), due to the lower vapor viscosity and higher velocity of the vapor phase. The "liquid-only" and "vapor-only" Reynolds numbers (Re_{lo}, Re_{vo}) provide benchmarks for assessing the dominance of each phase in momentum transport. Weber

Fig. 4. Distribution of the thermophysical properties of the database.
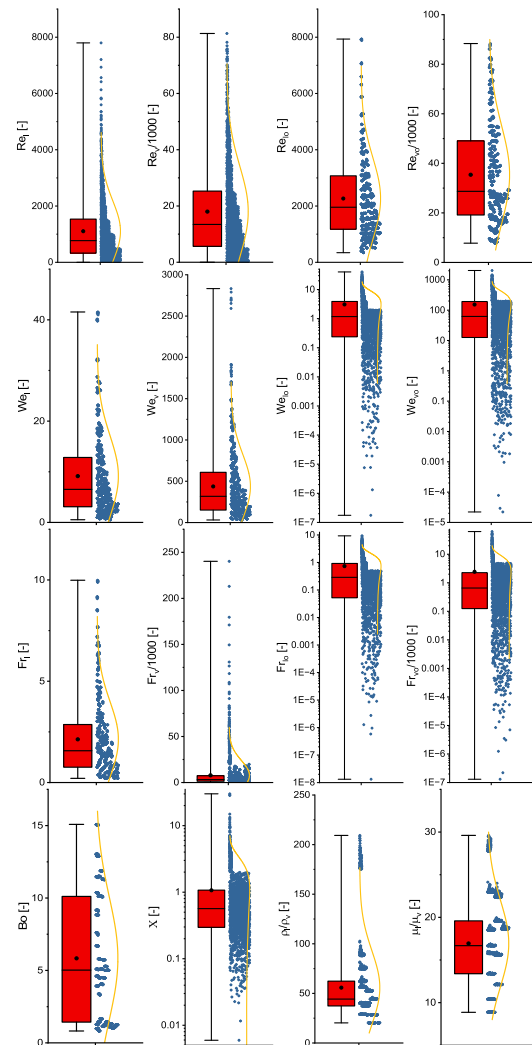
Fig. 5. Distribution of Renolds numbers, Weber number, Froude numbers with different two-phase definitions, with Bond number, Lockhart-Martinelli parameter (X), densities ratio, and viscosity ratios.

numbers (mean $We_l \sim 9$, $We_v \sim 436$, $We_{lo} \sim 3$, $We_{vo} \sim 135$) and Froude numbers (mean $Fr_l \sim 2$, $Fr_v \sim 7800$, $Fr_{lo} \sim 0.7$, $Fr_{vo} \sim 2700$) quantify the relative effects of inertia to surface tension and gravity, respectively. The high vapor-phase values indicate strong inertial dominance and are relevant to annular or dispersed flow, which are associated with higher pressure gradients. The Bond number (mean~5.8) reflects the balance between gravity and surface tension forces, so the values in this range suggest both effects are non-negligible in microchannel flow which influences phase distribution and stratification. The Lockhart-Martinelli parameter X (mean~1.07, but median~0.57) is a traditional indicator of two-phase flow regime and is directly used in classical pressure drop correlations, reinforcing its importance in the experimental investigation and the proposed new model. Large density and viscosity ratio enhance slip between phases and amplify phase distribution effects, which are significant for pressure gradient of two-phase flows.

Among these non-dimensional parameters, the Reynolds number and viscosity ratio measure the inertial and viscous effects. The Weber number and Bond number both use the surface tension, and they measure the interfacial phenomena. These parameters reflect the effect of flow patterns, bubbly dynamics, onset of flow pattern transitioning, and so on. The density ratio and Lockhart- Martinelli parameter are important for the phase distribution.

4. Pressure gradient measurements

4.1. Effect of vapor quality

Fig. 6 presents the measured two-phase pressure gradient (dP/dz) as a function of vapor quality (x) for five representative mass fluxes: 100, 150, 200, 250, and 300 kg m^{-2}s^{-1}. The results of R1234yf in a 2 mm tube at a saturation temperature of 5 °C are presented. For each mass flux, the corresponding data points span the full range of vapor quality from near zero (subcooled or saturated liquid) to values approaching 1 (saturated vapor). For all mass fluxes, the pressure gradient exhibits nearly a monotonic increase with vapor quality, with the increasing becoming more significant at higher mass flux and higher quality. The pressure gradient values are shown to basically increase with vapor quality. However, at extremely high vapor quality ($x > 0.95$), it seems that the pressure gradient decreases as quality increases. This is due to the absent of liquid and reduction in the interfacial friction between the vapor and liquid phases.

For a given mass flux, dP/dz increases with vapor quality, especially when x is less than 0.95. This behavior can be attributed to the reduction in liquid content (reduction in the two-phase flow density) and the associated increase in the two-phase flow velocity as quality rises.
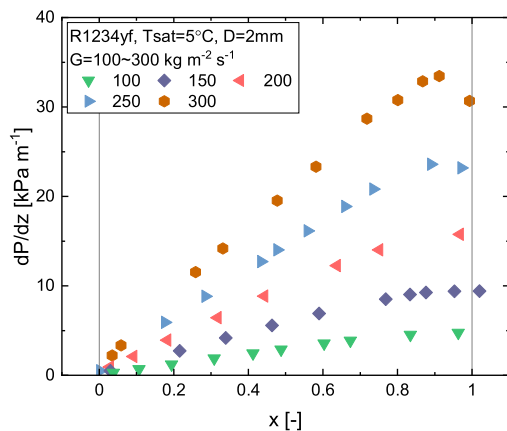
4.2. Effect of mass flux

The effect of mass flux on pressure gradient is also presented in Fig. 6. At the lowest mass flux (G ~ 100 kg m^{-2}s^{-1}), dP/dz increases modestly from ~0.29 kPa m^{-1} at x ~ 0 to a maximum of ~4.8 kPa m^{-} at x ~ 1. As mass flux increases, the magnitude of dP/dz at any given vapor quality also increases. For instance, at G ~ 200 kg m^{-2}s^{-1}, dP/dz rises from ~0.9 to ~15.8 kPa m^{-1}. At the highest mass flux (G ~ 300 kg m^{-2}s^{-1}), dP/dz values range from ~2.2 up to ~33.5 kPa m^{-1}, and ending at 30.67 kPa m^{-1} when x ~ 1. The dependence of pressure gradient on mass flux is nearly linear at low vapor quality, but it becomes stronger as vapor quality increases. When the mass flux is doubled from 100 to 200 kg m^{-2}s^{-1}, dP/dz increases by 231 %; and the increase is by 600 % when mass flux is tripled.

At any fixed vapor quality, the two-phase pressure gradient increases with mass flux. It seems that the quadratic dependence of frictional pressure drop on velocity is hold in both single-phase and two-phase flows. Using a simple curve fitting, it can be drawn that $dP/dz \propto G^{1.777}$. Higher mass fluxes imply higher superficial velocities of the two-phase refrigerant, increasing the shear at the wall and on the liquid-vapor interface, which amplifies the frictional losses and, consequently, the measured dP/dz. These trends are consistent with classical two-phase flow theory, in which frictional pressure drop is strongly influenced by both the total mass flux and the phase distribution within the tube [1,5].

4.3. Effect of saturation pressure

Fig. 7 displays the measured two-phase pressure gradient (dP/dz) as a function of vapor quality (x) for R1234yf flowing in a 2 mm internal diameter tube, at a fixed mass flux of about 150 kg m^{-2}s^{-1}. The results are presented for three distinct saturation temperatures: 5 °C, 15 °C, and 25 °C.

At 5 °C, the pressure gradient rises from 0.23 kPa m^{-1} at x = 0.01, reaching a maximum of 9.14 kPa m^{-1} at x = 0.96. At 15 °C, the initial dP/dz is 0.29 kPa m^{-1} (x = 0.02) and peaks at 6.76 kPa m^{-1} around x = 0.87, then decreases slightly at higher qualities, reaching 5.86 kPa m^{-1} at x = 1.11. At 25 °C, dP/dz starts at 0.33 kPa m^{-1} (x = 0.03) and increases to a maximum of 5.30 kPa m^{-1} at x = 0.92. At a given vapor quality, the pressure gradient decreases as saturation temperature increases. This trend is observed across the entire quality range. The reduction in dP/dz with increasing saturation temperature can be explained by thermophysical property changes. The density, especially the vapor density reduces at higher saturation temperature. So, when the temperature is lower, the two-phase flow velocity is higher.
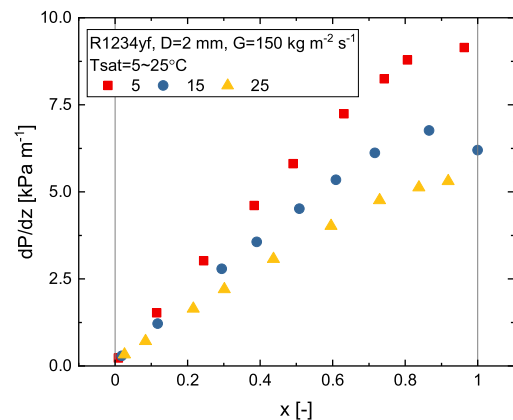

Fig. 6. Pressure gradient of R1234yf at varied mass flux from 100 to 300 kg m^{-2}s^{-1}.

Fig. 7. Pressure gradient of R1234yf at varied saturation temperature from 5 to 25 °C.

4.4. Effect of inner diameter

Fig. 8 illustrates the measured two-phase pressure gradient as a function of vapor quality (x) for R1234yf in tubes of three different internal diameters: 1 mm, 2 mm, and 3 mm. All tests are performed at a fixed mass flux (150 kg m^{-2}s^{-1}) and under 5 °C.

For the 1 mm tube, dP/dz increases steeply with vapor quality, from 1.12 kPa m^{-1} at x = 0.04 to a maximum of 22.3 kPa m^{-1} at x = 0.96. For the 2 mm tube, dP/dz increases from 0.23 kPa m^{-1} at x = 0.01 to a peak of 9.14 kPa m^{-1} at x = 0.96, then slightly declines at higher qualities. For the 3 mm tube, dP/dz rises more gradually with vapor quality, from 0.14 kPa m^{-1} at x = 0.01 to around 5.86 kPa m^{-1} at x = 0.92, with some fluctuation at superheated phase. For all tube sizes, the trend of increasing dP/dz with vapor quality is same to the other results. The absolute values and the rate of increase of dP/dz differ markedly with diameter. At a given mass flux and vapor quality, the pressure gradient is highest in the smallest tube (1 mm) and lowest in the largest (3 mm). A curve fitting shows that $dP/dz \propto D^{-1.224}$. The effect of diameter can be explained by the significant increasing in the surface area per unit volume flow and a strong effect in hydrodynamic scaling. The results confirm that in mini- and micro-scale tubes, the two-phase flow experiences high pressure gradients for a given mass flux. It indicates the significant constraints on the allowable flow rates when designing compact heat exchangers such as microchannel condensers and evaporators.

4.5. Effect of fluids (properties)

Fig. 9 compares the measured two-phase pressure gradient as a function of vapor quality for five different refrigerants: R1233zd(E), R1234ze(E), R1234yf, R134a, and R32, at a fixed mass flux (about 150 kg m^{-2}s^{-1}) and under the same tube diameter (2 mm) and temperature conditions (5 °C).

R1233zd(E) exhibits the highest pressure gradient across the full quality range, with dP/dz increasing steeply from 0.99 to 26.96 kPa m^{-1}. R1234ze(E) shows a moderate pressure gradient, with dP/dz rising from 0.31 to 14.04 kPa m^{-1}. R134a displays a intermediate pressure gradient, with dP/dz increasing from 0.63 to a peak of 8.4 kPa m^{-1}. R1234yf presents very similar behavior to R134a, but with slightly higher maximum dP/dz, ranging from 0.23 to 9.14 kPa m^{-1}. R32 has the lowest overall pressure gradient, with dP/dz increasing from 0.17 to 7.51 kPa m^{-1}, and a decline beyond x = 1.

R1233zd(E) (with the highest pressure gradient) has comparatively low vapor density and relatively high viscosity, resulting in greater phase slip and higher shear stress for a given testing condition. R1234ze (E) and R1234yf show lower dP/dz, benefiting from lower viscosity and higher vapor density, which reduce phase slip and frictional losses. R32
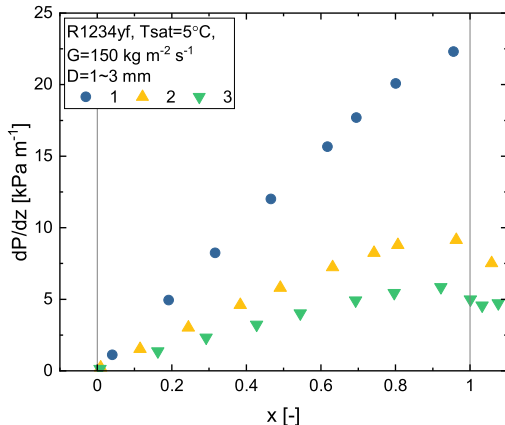

Fig. 8. Pressure gradient of R1234yf at varied inner diameter from 1 to 3 mm.
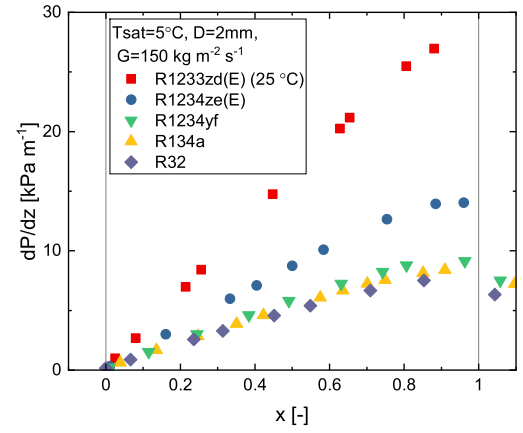

Fig. 9. Pressure gradient of five fluids: R32, R134a, R1234yf, R1234ze(E), and R1233zd(E).

has a relatively high saturation pressure and low molecular weight, and it also has the lowest pressure gradient. The results consistent with its high vapor density and low viscosity.

5. Development of a new predictive model

5.1. Evaluating method

This study examines the two-phase pressure gradient behavior of five refrigerants in 1, 2, and 3 mm tubes. To access the predictive capabilities of various pressure gradient models against the measured data, two primary statistical indicators are utilized: Mean Percentage Absolute Error (MPAE) and Mean Percentage Error (MPE).

$$MPAE = \frac{1}{N} \sum_{1}^{N} \frac{abs(Prediction - Measurement)}{Measurement} \times 100\% \qquad (7)$$

$$MPE = \frac{1}{N} \sum_{1}^{N} \frac{Prediction - Measurement}{Measurement} \times 100\% \qquad (8)$$

In addition, a residual analysis is performed to quantify the pointwise deviation between the prediction and measurements. The residual, R, is calculated as:

$$R = Measurement - Prediction \qquad (9)$$

A residual of zero denotes perfect agreement; negative and positive residuals correspond to overprediction and underprediction, respectively. Totest the sources of model error, correlation coefficients between the residual and major non-dimensional parameters (including Re_l, Re_v, Re_{lo}, Re_{vo}, We_l, We_v, We_{lo}, We_{vo}, Fr_l, Fr_v, Fr_{lo}, Fr_{vo}, Bo, X, ρ_l/ρ_v, and μ_l/μ_v) are computed and denoted as 'Cor(the non-dimensional parameter)'. For example, the correlation Cor(Re_l) between the liquid Reynolds number (Re_l) and the residual is calculated using the equation:

$$Cor(Re_l) = \frac{\sum_{1}^{N} (Re_{l,i} - \overline{Re_l})(R_i - \overline{R})}{\sqrt{\sum_{1}^{N} (Re_{l,i} - \overline{Re_l})^2} \sqrt{\sum_{1}^{N} (R_i - \overline{R})^2}} \qquad (10)$$

Here, the bar ($\overline{Re_l}$ and $\overline{R}$) means the averaged value, and the subscript i denotes the i th value.

5.2. Evaluation of the existing models

In this study, six models are evaluated and selected for their most accurate predictions (smallest MPAE). Among them, two of them are known as homogeneous model, that their equation for the homogeneous property is applied to the Blasius equation for predictions, and they are Cicchitti [23] and Akers [58]. The results are presented in Table 4 and

Table 4

Evaluation of the selected models.

Model	Kim and Mudawar [32]	Cicchitti [23]	Akers [58]	Qu and Mudawar [59]	Mishima and Hibiki [31]	Sempértegui-Tapia and Ribatski [60]
MPAE [%]	14.48	18.92	19.51	20.99	21.45	23.79
MPE [%]	3.11	−3.51	−14.49	1.38	12.78	22.62
$Cor(Re_l)$ [-]	−0.368	−0.146	−0.284	−0.549	−0.371	0.265
$Cor(Re_v)$ [-]	0.192	0.395	0.469	0.098	0.262	0.133
$Cor(Re_{lo})$ [-]	−0.219	0.199	0.058	−0.432	−0.180	0.346
$Cor(Re_{vo})$ [-]	−0.135	0.130	0.152	−0.334	−0.044	0.287
$Cor(We_l)$ [-]	−0.291	−0.134	−0.273	−0.465	−0.296	0.200
$Cor(We_v)$ [-]	0.325	0.416	0.567	0.256	0.432	0.043
$Cor(We_{lo})$ [-]	−0.145	0.203	0.148	−0.413	−0.091	0.230
$Cor(We_{vo})$ [-]	0.022	0.046	0.308	−0.157	0.180	0.068
$Cor(Fr_l)$ [-]	−0.305	−0.258	−0.286	−0.338	−0.150	−0.097
$Cor(Fr_v)$ [-]	0.838	0.228	0.728	0.771	0.867	−0.503
$Cor(Fr_{lo})$ [-]	0.183	0.162	0.393	0.021	0.395	−0.482
$Cor(Fr_{vo})$ [-]	0.421	−0.384	0.254	0.451	0.600	−0.613
$Cor(Bo)$ [-]	−0.290	0.064	−0.206	−0.360	−0.311	0.504
$Cor(X)$ [-]	−0.252	−0.151	−0.315	−0.217	−0.200	0.149
$Cor(\rho_l/\rho_v)$ [-]	0.335	−0.359	0.188	0.443	0.373	−0.337
$Cor(\mu_l/\mu_v)$ [-]	0.305	−0.285	0.142	0.365	0.317	−0.299

plotted in Fig. 10.

Among these six models, Kim and Mudawar [32] achieves the lowest MPAE (14.48 %), indicating the highest overall predictive accuracy among the six models. The MPE for Kim and Mudawar [32] is also very low, and the value is 3.11 %. It indicates that the overall bias is tiny. Cicchitti [23], Akers [58], Qu and Mudawar [59], and Mishima and Hibiki [31] display moderately higher MPAEs, ranging from 18.92 % to 21.45 %. Sempértegui-Tapia and Ribatski [60] yields the largest average error (MPAE = 23.79 %) and a strong positive bias (MPE = 22.62 %), suggesting a tendency toward substantial overprediction. Akers [58] and Cicchitti [23] tend to underpredict dP/dz (MPE = −14.49 % and

−3.51 %, respectively), while Sempértegui-Tapia and Ribatski [60] and Mishima and Hibiki [31] tend to overpredict (MPE = 22.62 % and 12.78 %, respectively). Qu and Mudawar [59] also has a small bias (MPE=1.38 %). These effects can all be observed from both the plot and table (Fig. 10 and Table 4) except for Mishima and Hibiki [31]. From the plot, it seems that the model is underpredicting dP/dz, against to the table. The reason is that the model overpredicts when dP/dz is low, and underpredicts when dP/dz is high. In the plot, it is easier to see the underprediction at high dP/dz values.

Kim and Mudawar [32] has strong positive correlation with vapor phase Froude number ($Cor(Fr_v) = 0.838$), indicating that errors increase
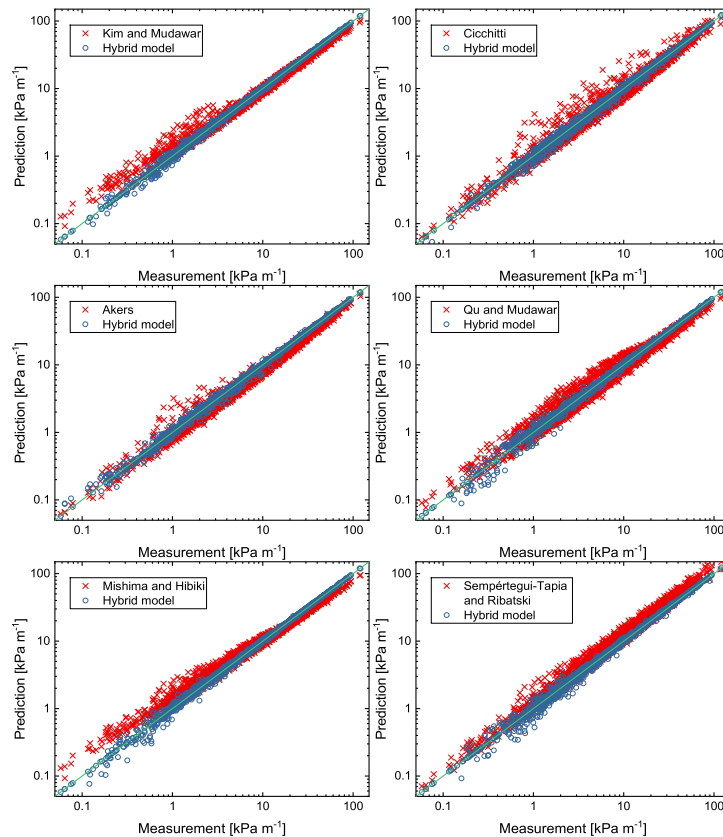
Fig. 10. Performance of the base models and new proposed hybrid models.

systematically with higher vapor-phase inertia. The model also has moderate negative correlation with liquid-phase Reynolds number (Cor $(Re_l) = -0.368$), suggesting underestimation in high Re_l conditions. Cicchitti [23] has positive correlation with vapor phase weber number (Cor$(We_v) = 0.416$) and vapor Reynolds number (Cor$(Re_v) = 0.395$), reflecting increased model error with more important vapor inertia. Akers [58] has moderate to strong positive correlation with the vapor phase Reynolds number (0.469), the vapor phase Weber number (0.567), and the vapor phase Froude number (0.728). It also has negative correlation with the liquid phase Reynolds number (−0.284). Qu and Mudawar [59] has strong negative correlation with the liquid phase Reynolds number (−0.549) and liquid phase Weber number (−0.465), suggesting underestimation at high liquid velocities and inertial conditions. It also has strong positive correlation with the vapor phase Froude number (0.771). Mishima and Hibiki [31] shows strong positive correlation with the vapor only Froude number (0.600) and vapor phase Froude number (0.867), and also with the liquid only Froude number (0.395). In addition, it has positive correlation with vapor phase Weber number (0.432). It seems this model's residual become increasingly positive with increasing vapor-phase inertial forces. Sempértegui-Tapia and Ribatski [60] shows strong negative correlations with liquid only and vapor only Froude numbers (cor(Fr_{lo})=−0.482, cor(Fr_{vo})=−0.613), as well as with the vapor phase Froude number (−0.503), indicating its systematic underestimation in high velocity conditions. It also has moderate positive correlation with the Bond number (0.504), suggesting the increasing residuals with stronger surface tension effects.

Among the six models, the vapor phase Froude number (Fr_v) is the most common parameter associated with strong correlation to model residuals, often exceeding 0.7 in absolute value for multiple models [32, 58,59,31]. This implies that errors in dP/dz prediction are most significant in flow conditions where vapor-phase inertia dominates, such as high vapor quality or high mass flux conditions. Another significantly positive correlation is with We_v and Re_v, and they are both positive in all six models. Again, it proves the importance of the effect of vapor quality

and mass flux on correcting the existing models.

All models show negative correlations with the liquid phase Reynolds number (Re_l) and liquid phase Weber number (We_l) except for Sempértegui-Tapia and Ribatski [60], but all six shows negative correlations with the liquid Froude number (Fr_l). This highlights the challenges in modeling pressure gradient where liquid phase dynamics are still significant. It might indicate the models need fine correction in low vapor quality.

The observation of the correlations show that Kim and Mudawar [32], Qu and Mudawar [59], and Mishima and Hibiki [31] have very similar trend. They have many commons in the sign of the correlations. Sempértegui-Tapia and Ribatski [60] is the most different model, it usually shows a negative correlations when other models show a positive value.

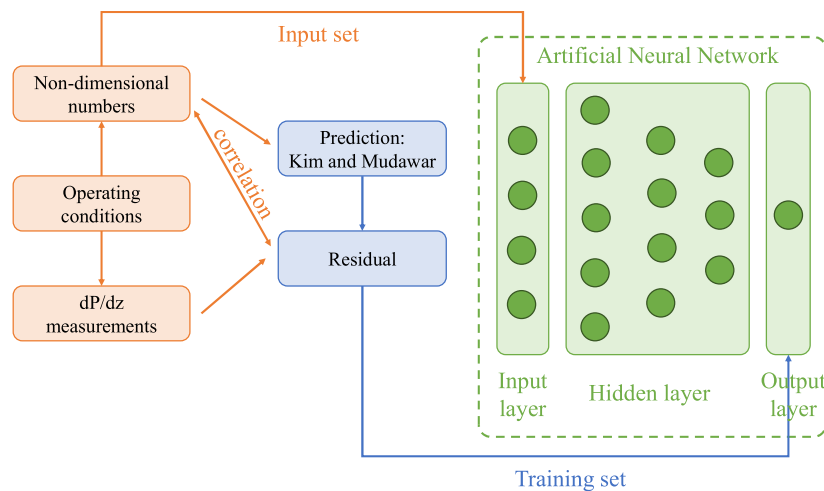### 5.3. Derive to the hybrid correlation-residual neural network (C-RNN)

5.3.1. Overview of the model

An illustration of how the new Hybrid Correlation-Residual Neural Network (C-RNN) model is developed, and application procedure is provided in Fig. 11.

The development of the model can be divided into several steps.

1) Collect the pressure gradient measurements and their testing (operating) conditions (such as vapor quality, pressure, mass flux, etc.).
2) Calculate the thermophysical properties from the testing conditions using a database, and then calculate the non-dimensional numbers relate to pressure gradient (such as Reynolds number, Weber number, Froude number, Bond number, etc.).
3) Predict pressure gradient using an existing model from the testing conditions and the thermophysical properties. In the figure, Kim and Mudawar [32] is listed as an example.
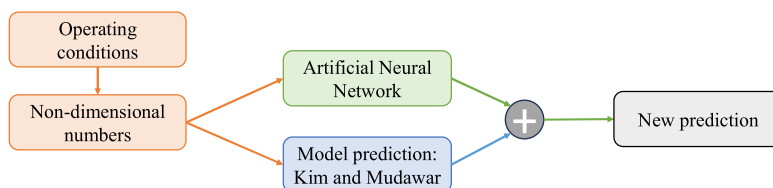

Fig. 11. The development and usage method of the new proposed Hybrid Correlation-Residual Neural Network model.

4) Calculate the residual of the model using Eq. (9) between the measurement collected from step 1) and the predicted dP/dz from step 3).

5) Calculate the correlation between the residual and the non-dimensional numbers using equation Eq. (10).

6) Rank the correlations calculated in the step 5) and find the several most important non-dimensional numbers.

7) Use the important non-dimensional numbers from step 6) as the input, the residual from step 4) as the output, train an artificial neural network.

The usage of the model is also divided into several steps.

1) Prepare the operating conditions (such as vapor quality, pressure, mass flux, etc.).

2) Calculate the thermophysical properties and non-dimensional numbers from the operating conditions.

3) Use the thermophysical properties and non-dimensional numbers on a predictive model (the figure use Kim and Mudawar [32] as an example) to calculate the dP/dz.

4) Use the artificial neural network to calculate the residual of the pressure gradient.

5) Use the calculated values from steps 3) and 4) to calculate the final predicted dP/dz.

The final form of the new proposed model is:

$$dP/dz = (\text{Prediction from existing model})$$
$$+ (\text{Residual from ANN model}) \qquad (11)$$

The other important thing on developing the new model is listed in to following subsections.

5.3.2. The important parameters

In the step 6), it needs to rank the important non-dimensional parameters (with the highest absolute correlation value). For example, the rank for Kim and Mudawar [32] are: Fr_v, Fr_{vo}, Re_l, ρ_l/ρ_v, We_v, μ_l/μ_v, Fr_l, We_l, Bo, X, Re_{lo}, Re_v, Fr_{lo}, We_{lo}, Re_{vo}, We_{vo}. The same procedure is applied to the other four models (Cicchitti [23], Akers [58], Qu and Mudawar [59], Mishima and Hibiki [31], Sempértegui-Tapia and Ribatski [60]).

5.3.3. Training the neural network

An Artificial Neural Network (ANN) model is trained to predict the residuals between experimental measurements and correlation-based predictions using the model parameters listed in Table 5.

The compiled experimental dataset consists of five refrigerants (R1234yf, R134a, R1234ze(E), R32, and R1233zd(E)). The ANN employed for residual modeling is trained using the Adam optimizer. For ANN development, the dataset is randomly divided into 70 % training, 15 % validation, and 15 % testing subsets. In total, the hybrid ANN is trained and validated on 1425 data points, with 997 points for training,

Table 5
ANN model parameters.

Parameter	Value/Description
Activation function	ReLU (all hidden layers)
Loss function	Mean Squared Error (MSE)
Regularization	L2
L2 regularization parameter	0.001
Optimizer/Solver	Adam
Batch size	200
Initial learning rate	0.001
Exponential decay rate β_1	0.9
Exponential decay rate β_2	0.999
Maximum epochs	1000
Data split (train/validation/test)	70 % / 15 % / 15 %
Input normalization	z-score ((input - mu) / sigma)

214 for validation, and 214 for testing. The training set is used to fit the network weights, the validation set is used to monitor generalization error and prevent overfitting, and the test set is reserved for final performance evaluation. To ensure reproducibility, the partitioning is performed programmatically with a fixed random seed, guaranteeing that the same samples are used in each subset across all training runs. The layers use the ReLU activation function. The training targets the minimization of Mean Squared Error (MSE) loss, with L2 regularization (0.001) applied to mitigate overfitting. Training is performed in mini-batches of 200 samples, with an initial learning rate of 0.001. The Adam optimizer parameters for exponential decay rates are set to $\beta_1 = 0.9$ and $\beta_2 = 0.999$, following standard best practices. Training is terminated once the improvement in loss fell below a tolerance of 0.001 or after reaching the maximum number of epochs (1000). The convergence behavior is assessed by plotting the MSE versus training iteration.

$$MSE = \frac{1}{N} \sum_{1}^{N} (prediction - measurement)^2 \qquad (12)$$
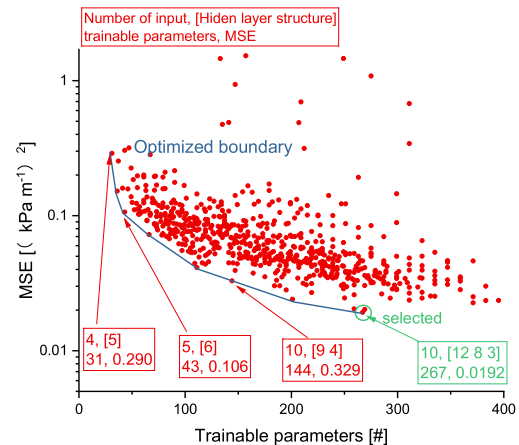
5.3.4. The optimized neural network structure

To maximize the predictive performance of the residual neural network for each base correlation, a structured search is conducted over input sets (4–12 physically motivated, non-dimensional groups) and architectures (from a single hidden layer with 5 neurons to three hidden layers with descending widths, e.g., [12 11 10]). Feature candidates are selected from prior correlation analysis (Section 5.2) and physical relevance.

For each candidate input sets and architectures, the networks are trained and validated using the same dataset (with the same random seed on dividing the training, testing, and validating sets). The Mean Squared Error (MSE) of the ANN model prediction and the total trainable parameters are jointly considered for selecting the optimal structure. Lower MSE indicates higher prediction accuracy, while the number of trainable paymasters is a complexity measure of the network structure. The training time is also presented, and it reflects the computational efficiency. For example, four structures are selected as the optimized for Kim and Mudawar [32] and they are presented in Fig. 12.

The performance of all tested neural network configurations was visualized on a two-dimensional plot of MSE versus trainable parameters, as shown in Fig. 12. The optimized boundary (Pareto front) is identified to represent the set of models offering the best trade-off between accuracy and structure complexity. There are four structures that are very close to the optimized boundary in the figure. The structure with the smallest MSE and on the optimized boundary is selected for further development of the model, and in Fig. 12 it is [12 8 3] as hidden

Fig. 12. Performance of all tested neural networks and the selected four network structures for further testing. In this plot, the training results for residual of Kim and Mudawar [32] is showed as an example.

layer, and the input set contains the most 10 important non-dimensional numbers. The results of the other five base models are listed in Appendix A.

The final selected architectures for each base model are summarized in Table 6. For each case, the chosen network structure (input count, hidden layers), corresponding MSE, training time, number of parameters, and final predictive metrics (MPAE and MPE) are reported. The MPAEs are also extended to include training, validation, and test sets, as presented in Table 7. All selected networks employed multi-layer architectures with 10 to 12 input features and three hidden layers. The predictions (from the new hybrid model) against measurements are also plotted in Fig. 10 compared to the original base model. It proves the accuracy of the new hybrid model because of that all the results are aligned with the 45-degree line.

While deeper and larger networks with more parameters were also tested (up to ~370 trainable parameters and 1000 epochs), they did not necessarily yield the lowest error. Instead, the final architectures were chosen based on the lowest MPAE on the independent test set, ensuring that both predictive accuracy and generalization were optimized.

5.4. Performance of the new model

The new proposed Hybrid Correlation-Residual Neural Network model is tested and plotted against the measurements in Fig. 13. Results are presented for R1234yf at two mass fluxes (150 and 300 kg m^{-2}s^{-1}) and two tube diameters (1 mm and 2 mm), for two different saturation temperatures (5 °C and 25 °C), as well as for R32 at 150 kg m^{-2}s^{-1} and 2 mm diameter at 5 °C. Therefore, this comparison proves the accuracy of the new proposed model with varied refrigerant type, mass flux, saturation condition, and tube diameters.

The new model predictions closely follow the experimental data for all tested refrigerants and operating conditions. Both the magnitude and the curvature of the predicted dP/dz as a function of vapor quality accurately reflect the measured trends.

For reference, the correlation-informed neural network (CINN) proposed by Montañez-Barrera et al. [52] is also reproduced for benchmarking. The original model uses a different range of testing conditions for this study, therefore, the CINN architecture is retrained on the present experimental dataset using the same hyper-parameters reported in the original paper. The retrained CINN achieves an MPAE of 7.6 %, closely matching the performance of the proposed hybrid C-RNN (5.6 %), and both substantially improve upon traditional correlations (15–24 %). The comparison is presented in Fig. 14.

To further assess the generalization ability of the proposed hybrid model, an extrapolation test is conducted using an external experimental dataset reported by six external sources (the data is not included in the modeling process in this study). The comparison is presented in Fig. 15 and details of each source and the performance are quantitated in Table 8. The baseline Kim and Mudawar [32] yields an overall MPAE of 139 %, while the proposed C-RNN improves the MPAE to 104 %, confirming that the hybrid approach effectively improves predictive accuracy even under external operating conditions not included in the training database. The new proposed hybrid C-RNN model shows good potential to improve the prediction when the working conditions are similar to this study (comparing Monroe [61]). In addition, for those

Table 7
Results of per-split MPAEs.

Base Model	Whole MPAE [%]	Training [%]	Validation [%]	Test [%]
Kim and Mudawar [32]	5.60	4.57	6.86	9.14
Cicchitti [23]	9.67	7.89	11.84	15.79
Akers [58]	4.8	3.92	5.88	7.84
Qu and Mudawar [59]	6.18	5.05	7.57	10.09
Mishima and Hibiki [31]	4.95	4.04	6.06	8.08
Sempértegui-Tapia and Ribatski [60]	8.54	6.97	10.46	13.94
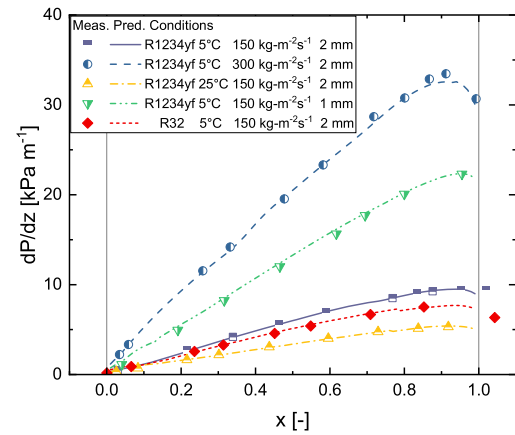
Fig. 13. Pressure gradient prediction of the new proposed hybrid model (using Kim and Mudawar [32] as the base model as an example).
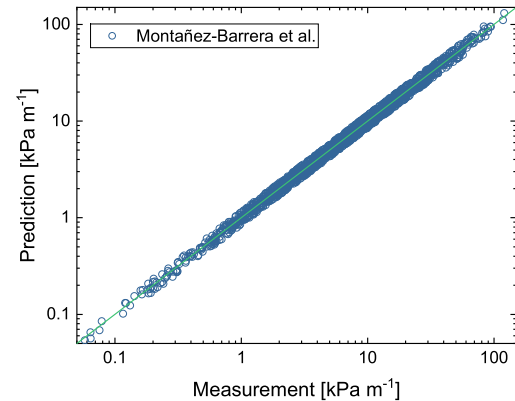
Fig. 14. The performance of the CINN approach proposed by Montañez-Barrera et al. (retrained) [52].

studies that the ranges are different, the proposed model also improves the accuracy. For the studies with extremely high MPAE (Ducoulombier et al. [62], Yun et al. [63], and Chang et al. [64]), the inaccurate predictions all appear at very low vapor quality (for example, in Chang et al. [64], when x = 0.1, 0.2, 0.3, and 0.4, the absolute errors=4500, 2279,

Table 6
The selected structure of each base model.

| Base Model	Input	Hidden layer	No. of parameters	MSE [kPa^2 m^{-2}]	Training time [s]	MPAE [%]	MPE [%]
Kim and Mudawar [32]	10	[12 8 3]	267	0.0192	8.360	5.60	0.33
Cicchitti [23]	12	[12 10 6]	359	0.1710	8.236	9.67	−0.02
Akers [58]	12	[10 8 5]	269	0.0378	8.210	4.80	0.58
Qu and Mudawar [59]	12	[12 8 7]	331	0.0427	7.022	6.18	−0.22
Mishima and Hibiki [31]	11	[12 10 8]	371	0.0196	8.296	4.95	0.06
Sempértegui-Tapia and Ribatski [60]	10	[12 8 6]	297	0.0563	8.240	8.54	2.27
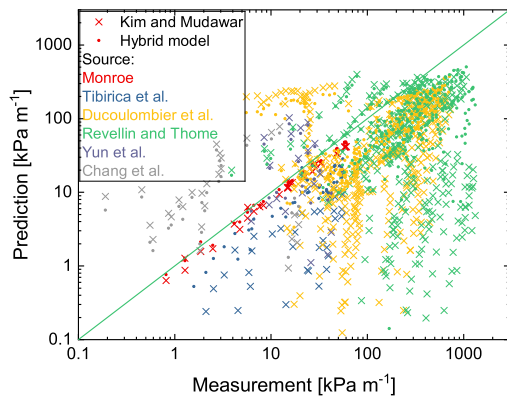
Fig. 15. Comparison of the proposed C-RNN model to the six sources (which was not included in the model development).

284, and 403 % for Kim and Mudawar [32], and the hybrid model improves errors to 2908, 1800, 171, 290 %, respectively).

5.5. Discussion on the hybrid correlation-residual neural network model

The achieved accuracy of the proposed C-RNN (average MPAE~6 %) is comparable to the performance of other correlation-informed ANN models (also ~6 %, Montañez-Barrera et al. [48]) and substantially better than purely neural network models, which report MPAEs between 16.8–82.7 % (Mauro et al. [47]). Using an external source of data not included in the training [61], it improved the MPAE from 22.7 % to 11.0 %. This confirms that coupling physics-based correlations with residual learning provides a more robust and generalizable predictive framework than either correlations or ANNs alone.

The principal strength of the proposed hybrid correlation-residual neural network model lies in its integration of physics-based understanding with data-driven refinement. By employing a well-established physical correlation as the primary predictive baseline and using the neural network to correct the residuals, the model ensures that predictions follow the governing principles of two-phase flow. This hybrid approach leverages the interpretability and generalizability of mechanistic models, while the neural network adaptively learns and corrects the systematic deviations. Consequently, the C-RNN model not only preserves physical realism but also achieves significantly enhanced predictive accuracy across a wide range of operating conditions and refrigerant types.

The value of the C-RNN methodology extends beyond predictive accuracy improvement. In commercial simulation platforms such as AMESIM, empirical pressure gradient or heat transfer coefficient correlation is tuned using one constant correction factor in the calibration process of heat exchanger. However, such static adjustments cannot account for the complex, nonlinear dependencies of two-phase flow behavior on flow regime, geometry, and fluid properties. It may

frequently result in systematic overprediction under certain conditions and underprediction under the other conditions. By contrast, the Correlation-Residual Neural Network can be efficiently trained on personal computing resources and easily embedded within existing simulation environments.

In the future, the usage of the C-RNN approach opens several promising avenues for further research and application. An immediate next step is to extend to the prediction of other key performance parameters, such as the local heat transfer coefficient in both boiling and condensing regimes. By developing the hybrid models for heat transfer, it will be possible to achieve a unified, physically informed, and data-enhanced modeling approach capable of supporting next-generation component and system design in thermal-fluid applications. In addition, trying to integrate the hybrid model into component-level (heat exchanger-level) simulations enables comprehensive performance evaluation and optimization of complete refrigeration or air conditioning systems.

6. Conclusion

This study presents a comprehensive experimental and modeling investigation of two-phase pressure gradient in small diameter tubes with various refrigerants. A Hybrid Correlation-Residual Neural Network (C-RNN) model is developed, integrating physics-based correlations with data-driven correction to enhance predictive accuracy. The experimental investigation covers a wide range of operating conditions, and the new modeling approach is validated against extensive measurement data.

The database includes five refrigerants (R1234yf, R134a, R1234ze (E), R32, and R1233zd(E)) in round tubes of 1–3 mm diameter, with mass flux from 100 to 300 kg m^{-2}s^{-1} and saturation temperatures from 5 °C to 25 °C.

Experimental results confirm that the two-phase pressure gradient increases strongly with both vapor quality and mass flux, and is highly sensitive to tube diameter and refrigerant properties. Pressure gradient increases by six times when mass flux is tripled. In addition, reducing the tube diameter from 3 mm to 1 mm increases dP/dz by nearly a factor of four. Notably, small diameters and lower density refrigerants result in higher dP/dz.

Among conventional models, significant, systematic residuals are observed and analyzed, particularly at high vapor qualities and high mass fluxes, especially for vapor-dominated flow regimes. This indicates the need for more flexible predictive frameworks.

The proposed hybrid C-RNN model, which uses a mechanistic correlation as a baseline and an artificial neural network for residual correction, demonstrates excellent agreement with measured data across all tested conditions. The model accurately captures nonlinear effects of the fluid properties and operating conditions. Across the five base correlations tested, the C-RNN reduces the mean percentage absolute error (MPAE) from values as high as 19–24 % down to 4.8–9.7 %, with the best case achieving MPAE = 4.8 % and MPE close to zero. The

Table 8
The six external sources for comparison.

Sources	Fluid(s)	Tube diameter [mm]	Mass flux [kg m^{-2}s^{-1}]	Saturation condition	No. of data points	MPAE of Kim and Mudawar [%]	MPAE of the hybrid C-RNN model [%]
Monroe [61]	R134a	1.66	50–400	350	32	22.7	11.0
Tibirica and Ribatski [65]	R245fa	2.32	100–700	185–260	39	82.3 %	57.1 %
Ducoulombier et al. [62]	R744	0.529	200–1410	2600–4000	337	162 %	117 %
Revellin and Thome [66]	R134a, R245fa	0.509	350–2000	20, 35 °C	296	83.7 %	71.4 %
Yun et al. [63]	R410A	1.44	200–400	0–10 °C	19	149 %	116 %
Chang et al. [64]	R410A	5	200–400	5, 25 °C	27	677 %	490 %
All					**750**	**139 %**	**104 %**

new model reduces both mean and absolute error metrics compared to standalone empirical correlations.

CRediT authorship contribution statement

Houpei Li: Writing – original draft, Methodology, Investigation, Formal analysis, Conceptualization. **Lei Wang:** Writing – review & editing, Validation. **Wenzhe Li:** Writing – review & editing, Investigation.

Declaration of competing interest

The authors declare that they have no known competing financial interests or personal relationships that could have appeared to influence the work reported in this paper.

Appendix A

This appendix shows the performance of all tested neural networks of the five base models that are not used as example in the main text. Fig. A1, Fig. A2, Fig. A3, Fig. A4, Fig. A5.
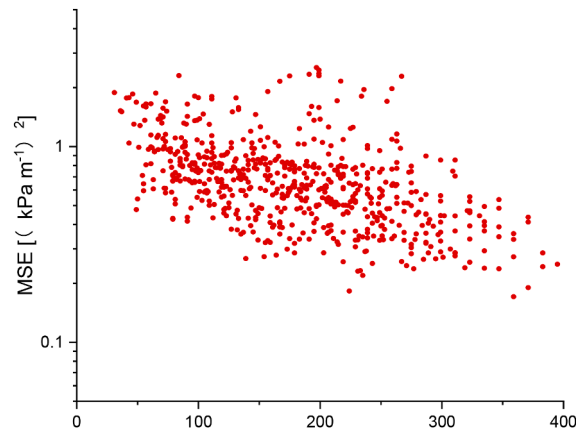

Fig. A.1. performance of all tested neural networks using Cicchitii as the base model.
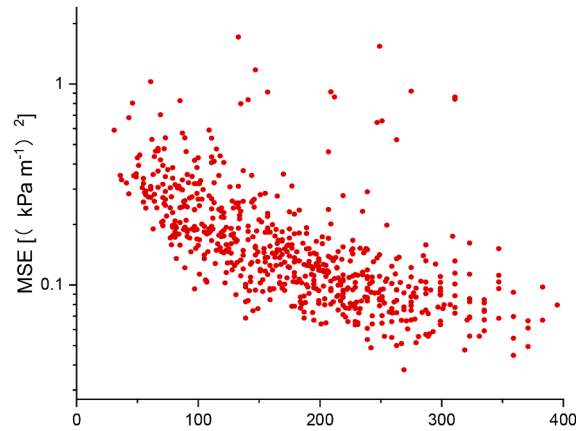

Fig. A.2. performance of all tested neural networks using Akers as the base model.
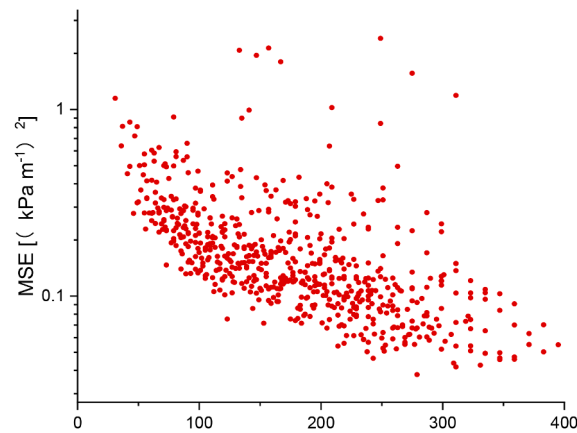
Fig. A.3. performance of all tested neural networks using Qu and Mudawar as the base model.
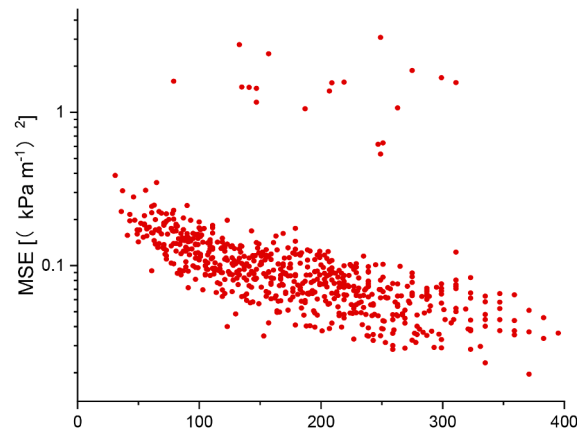

Fig. A.4. performance of all tested neural networks using Mishima and Hibiki as the base model.
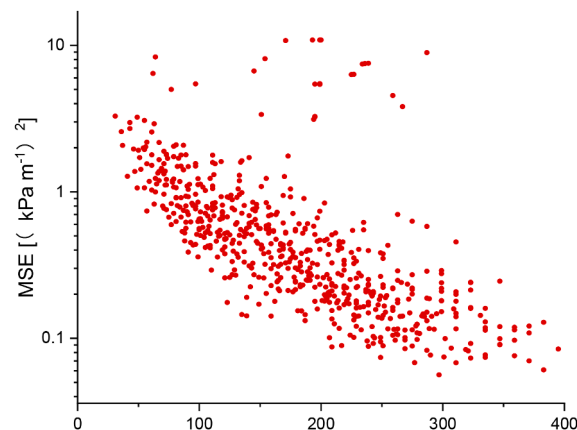

Fig. A.5. performance of all tested neural networks using Sempértegui-Tapia and Ribatski as the base model.

Data availability

The authors do not have permission to share data.

References

[1] F. de Rossi, A.W. Mauro, A. Rosato, Local heat transfer coefficients and pressure gradients for R-134a during flow boiling at temperatures between −9°C and + 20°C, Energy Convers. Manag. 50 (2009) 1714–1721, https://doi.org/10.1016/j.enconman.2009.03.022.

[2] Lili Feng, Experimental Study of Reversible AC/HP System for Electric Vehicles, Ph.D Thesis, University of Illinois at Urbana-Champaign, 2019.

[3] M.M. Shah, Unified correlation for heat transfer during boiling in plain mini/micro and conventional channels, Int. J. Refrig. 74 (2017) 606–626, https://doi.org/10.1016/j.ijrefrig.2016.11.023.

[4] Y. Zou, P.S. Hrnjak, Single-phase and two-phase flow pressure drop in the vertical header of microchannel heat exchanger, Int. J. Refrig. 44 (2014) 12–22, https://doi.org/10.1016/j.ijrefrig.2014.05.007.

[5] S.-M. Kim, I. Mudawar, Review of databases and predictive methods for pressure drop in adiabatic, condensing and boiling mini/micro-channel flows, Int. J. Heat Mass Transf. 77 (2014) 74–97, https://doi.org/10.1016/j.ijheatmasstransfer.2014.04.035.

[6] I.H. Bell, P.A. Domanski, M.O. McLinden, G.T. Linteris, The hunt for nonflammable refrigerant blends to replace R-134a, Int. J. Refrig. 104 (2019) 484–495, https://doi.org/10.1016/j.ijrefrig.2019.05.035.

[7] C.-Y. Yang, H. Nalbandian, F.-C. Lin, Flow boiling heat transfer and pressure drop of refrigerants HFO-1234yf and HFC-134a in small circular tube, Int. J. Heat Mass Transf. 121 (2018) 726–735, https://doi.org/10.1016/j.ijheatmasstransfer.2017.12.161.

[8] K. Taddonio, N. Sherman, S.O. Andersen, Next Generation Refrigerant Transition: Lessons Learned from Automotive Industry Experiences with CFC-12, HFC-134a and HFO-1234yf, 2019, https://doi.org/10.4271/2019-01-0909, 2019-01–0909.

[9] H. Li, K. Tang, A comprehensive study of drop-in alternative mixtures for R134a in a mobile air-conditioning system, Appl. Therm. Eng. 203 (2022) 117914, https://doi.org/10.1016/j.applthermaleng.2021.117914.

[10] K.M. Karber, O. Abdelaziz, E.A. Vineyard, Experimental Performance of R-1234yf as a Drop-in Replacement for R-134a in Domestic Refrigerators, 2012, p. 11.

[11] S. Fukuda, C. Kondou, N. Takata, S. Koyama, Low GWP refrigerants R1234ze(E) and R1234ze(Z) for high temperature heat pumps, Int. J. Refrig. 40 (2014) 161–173, https://doi.org/10.1016/j.ijrefrig.2013.10.014.

[12] J. Yang, Z. Ye, B. Yu, H. Ouyang, J. Chen, Simultaneous experimental comparison of low-GWP refrigerants as drop-in replacements to R245fa for Organic Rankine cycle application: r1234ze(Z), R1233zd(E), and R1336mzz(E), Energy 173 (2019) 721–731, https://doi.org/10.1016/j.energy.2019.02.054.

[13] H. Fazelnia, S. Azarhazin, B. Sajadi, M.A.A. Behabadi, S. Zakeralhoseini, M. V. Rafieinejad, Two-phase R1234yf flow inside horizontal smooth circular tubes: heat transfer, pressure drop, and flow pattern, Int. J. Multiph. Flow 140 (2021) 103668, https://doi.org/10.1016/j.ijmultiphaseflow.2021.103668.

[14] J. Garcia Pabon, A. Khosravi, R. Nunes, L. Machado, Experimental investigation of pressure drop during two-phase flow of R1234yf in smooth horizontal tubes with internal diameters of 3.2 mm to 8.0 mm, Int. J. Refrig. 104 (2019) 426–436, https://doi.org/10.1016/j.ijrefrig.2019.05.019.

[15] H. Li, P. Hrnjak, Heat transfer coefficient, pressure gradient, and flow patterns of R1234yf evaporating in microchannel tube, J. Heat Transf. 143 (2021) 042501, https://doi.org/10.1115/1.4049635.

[16] H. Li, P. Hrnjak, Measurement of heat transfer coefficient and pressure drop during evaporation of R134a in new type facility with one pass flow through microchannel tube, Int. J. Heat Mass Transf. 115 (2017) 502–512, https://doi.org/10.1016/j.ijheatmasstransfer.2017.07.066.

[17] A. Arcasi, R. Mastrullo, A.W. Mauro, L. Viscito, Adiabatic frictional pressure gradient during flow boiling of pure refrigerant R1233zd and non-azeotropic mixtures R448A, R452A and R455A, J. Phys. 2177 (2022) 012045, https://doi.org/10.1088/1742-6596/2177/1/012045.

[18] H. Huang, N. Borhani, J.R. Thome, Experimental investigation on flow boiling pressure drop and heat transfer of R1233zd(E) in a multi-microchannel evaporator, Int. J. Heat Mass Transf. 98 (2016) 596–610, https://doi.org/10.1016/j.ijheatmasstransfer.2016.03.051.

[19] F. Ramírez-Rivera, A. López-Belchí, F. Vera-García, J.R. García-Cascales, F. Illán-Gómez, Two phase flow pressure drop in multiport mini-channel tubes using R134a and R32 as working fluids, Int. J. Therm. Sci. 92 (2015) 17–33, https://doi.org/10.1016/j.ijthermalsci.2015.01.014.

[20] G. Righetti, G.A. Longo, C. Zilio, R. Akasaka, S. Mancin, R1233zd(E) flow boiling inside a 4.3 mm ID microfin tube, Int. J. Refrig. 91 (2018) 69–79, https://doi.org/10.1016/j.ijrefrig.2018.04.020.

[21] A. Cavallini, D. Del Col, M. Matkovic, L. Rossetto, Pressure drop during two-phase flow of R134a and R32 in a single minichannel, J. Heat Transf. 131 (2009) 033107, https://doi.org/10.1115/1.3056556.

[22] J.A. Morrow, M.M. Derby, Flow condensation heat transfer and pressure drop of R134a alternative refrigerants R513A and R450A in 0.95-mm diameter minichannels, Int. J. Heat Mass Transf. 192 (2022) 122894, https://doi.org/10.1016/j.ijheatmasstransfer.2022.122894.

[23] A. Cicchitti, C. Lombardi, M. Silvestri, G. Soldaini, R. Zavattarelli, Two-Phase Cooling Experiments: Pressure Drop, Heat Transfer And Burnout Measurements, Centro Informazioni Studi Esperienze, Milan, 1959. https://www.osti.gov/biblio/4181977 (Accessed 29 September 2022).

[24] W.H. McAdams, Vaporization inside horizontal tubes-II, Benzene oil mixtures, Trans. ASME 64 (1942) 193–200.

[25] A.E. Dukler, M. Wicks, R.G. Cleveland, Frictional pressure drop in two-phase flow: B. An approach through similarity analysis, AIChE J. 10 (1964) 44–51, https://doi.org/10.1002/aic.690100118.

[26] D.R.H. Beattie, P.B. Whalley, A simple two-phase frictional pressure drop calculation method, Int. J. Multiph. Flow 8 (1982) 83–87, https://doi.org/10.1016/0301-9322(82)90009-X.

[27] C.B. Tibiriçá, D.M. Rocha, I.L.S. Sueth, G. Bochio, G.K.K. Shimizu, M.C. Barbosa, S. D.S. Ferreira, A complete set of simple and optimized correlations for microchannel flow boiling and two-phase flow applications, Appl. Therm. Eng. 126 (2017) 774–795, https://doi.org/10.1016/j.applthermaleng.2017.07.161.

[28] R.W. Lockhart, R.C. Martinelli, Proposed correlation of data for isothermal two-phase, two-component flow in Pipes.pdf, Chem. Eng. Prog. 45 (1949) 39–48.

[29] Lutz Friedel, Improved friction pressure drop correlation for horizontal and vertical two-phase pipe flow, in: Proc Eur. Two-Phase Flow Group Meet, Ispra, Italy, 1979.

[30] D. Chisholm, Two-Phase Flow in Heat Exchangers and Pipelines, Heat. Transf. Eng 6 (1985) 48–57, https://doi.org/10.1080/01457638508939624.

[31] K. Mishima, T. Hibiki, Some characteristics of air-water two-phase flow in small diameter vertical tubes, Int. J. Multiph. Flow 22 (1996) 703–712, https://doi.org/10.1016/0301-9322(96)00010-9.

[32] S.-M. Kim, I. Mudawar, Universal approach to predicting two-phase frictional pressure drop for adiabatic and condensing mini/micro-channel flows, Int. J. Heat Mass Transf. 55 (2012) 3246–3261, https://doi.org/10.1016/j.ijheatmasstransfer.2012.02.047.

[33] L. Sun, K. Mishima, An evaluation of prediction methods for saturated flow boiling heat transfer in mini-channels, Int. J. Heat Mass Transf. 52 (2009) 5323–5329, https://doi.org/10.1016/j.ijheatmasstransfer.2009.06.041.

[34] H. Li, P. Hrnjak, Experimental study of R448A flow boiling in a 24-port microchannel tube, Int. J. Refrig. 158 (2024) 238–252, https://doi.org/10.1016/j.ijrefrig.2023.11.010.

[35] H. Müller-Steinhagen, K. Heck, A simple friction pressure drop correlation for two-phase flow in pipes, Chem. Eng. Process. Process Intensif. 20 (1986) 297–308, https://doi.org/10.1016/0255-2701(86)80008-3.

[36] H. Li, P. Hrnjak, A mechanistic model in annular flow in microchannel tube for predicting heat transfer coefficient and pressure gradient, Int. J. Heat Mass Transf. 203 (2023) 123805, https://doi.org/10.1016/j.ijheatmasstransfer.2022.123805.

[37] B.S. Field, P. Hrnjak, A mechanistic model of two-phase pressure drop in microchannels, in: Vol. 6 Fluids Therm. Syst. Adv. Process Ind. Parts B, ASMEDC, Denver, Colorado, USA, 2011, pp. 411–419, https://doi.org/10.1115/IMECE2011-64269.

[38] J.R. Thome, J. El Hajal, A. Cavallini, Condensation in horizontal tubes, part 2: new heat transfer model based on flow regimes, Int. J. Heat Mass Transf. 46 (2003) 3365–3387, https://doi.org/10.1016/S0017-9310(03)00140-6.

[39] A.M. Jacobi, J.R. Thome, Heat transfer model for evaporation of elongated bubble flows in microchannels, J. Heat Transf. 124 (2002) 1131–1136, https://doi.org/10.1115/1.1517274.

[40] M. Magnini, J.R. Thome, An updated three-zone heat transfer model for slug flow boiling in microchannels, Int. J. Multiph. Flow 91 (2017) 296–314, https://doi.org/10.1016/j.ijmultiphaseflow.2017.01.015.

[41] A.W. Mauro, A.F. Passarelli, F. Pelella, L. Viscito, A mechanistic predictive model for pressure drop and void fraction calculation in two-phase flows and annular flow regime, Exp. Therm. Fluid Sci. 170 (2026) 111590, https://doi.org/10.1016/j.expthermflusci.2025.111590.

[42] X. Li, N. Li, X. Lei, R. Liu, Q. Fang, B. Chen, Study on artificial neural network for predicting gas-liquid two-phase pressure drop in pipeline-riser system, Energies 16 (2023) 1686, https://doi.org/10.3390/en16041686.

[43] Z. Li, G. Lin, C. Dong, H. Liang, Y. Xu, Prediction of the heat transfer coefficient and frictional pressure drop for flow boiling of environmentally friendly refrigerants based on an artificial neural network, Int. J. Heat Mass Transf. 252 (2025) 127428, https://doi.org/10.1016/j.ijheatmasstransfer.2025.127428.

[44] A. Haghighi, M.S. Shadloo, A. Maleki, M.Y. Abdollahzadeh Jamalabadi, Using committee neural network for prediction of pressure drop in two-phase microchannels, Appl. Sci. 10 (2020) 5384, https://doi.org/10.3390/app10155384.

[45] A. Khosravi, J.J.G. Pabon, R.N.N. Koury, L. Machado, Using machine learning algorithms to predict the pressure drop during evaporation of R407C, Appl. Therm. Eng. 133 (2018) 361–370, https://doi.org/10.1016/j.applthermaleng.2018.01.084.

[46] B.-L. Chen, T.-F. Yang, U. Sajjad, H.M. Ali, W.-M. Yan, Deep learning-based assessment of saturated flow boiling heat transfer and two-phase pressure drop for evaporating flow, Eng. Anal. Bound. Elem. 151 (2023) 519–537, https://doi.org/10.1016/j.enganabound.2023.03.016.

[47] A.W. Mauro, R. Revellin, L. Viscito, Development and assessment of performance of artificial neural networks for prediction of frictional pressure gradients during two-phase flow, Int. J. Heat Mass Transf. 221 (2024) 125106, https://doi.org/10.1016/j.ijheatmasstransfer.2023.125106.

[48] Y. Qiu, D. Garg, L. Zhou, C.R. Kharangate, S.-M. Kim, I. Mudawar, An artificial neural network model to predict mini/micro-channels saturated flow boiling heat transfer coefficient based on universal consolidated data, Int. J. Heat Mass Transf. 149 (2020) 119211, https://doi.org/10.1016/j.ijheatmasstransfer.2019.119211.

[49] J. Wang, Enhanced Flow Boiling Heat Transfer Performance of Diamond Microchannels: An Experimental Study, 2025.

[50] A.B. Buhendwa, S. Adami, N.A. Adams, Inferring Incompressible Two-Phase Flow Fields From the Interface Motion Using Physics-Informed Neural Networks, 2021, https://doi.org/10.48550/arXiv.2101.09833.

[51] D. Jalili, Y. Mahmoudi, Physics-informed neural networks for two-phase film boiling heat transfer, Int. J. Heat Mass Transf. 241 (2025) 126680, https://doi.org/10.1016/j.ijheatmasstransfer.2025.126680.

[52] J.A. Montanez-Barrera, J.M. Barroso-Maldonado, A.F. Bedoya-Santacruz, A. Mota-Babiloni, Correlated-informed neural networks: a new machine learning framework to predict pressure drop in micro-channels, Int. J. Heat Mass Transf. 194 (2022) 123017, https://doi.org/10.1016/j.ijheatmasstransfer.2022.123017.

[53] A.F. Passarelli, R. Mastrullo, R. Revellin, L. Viscito, A.W. Mauro, Estimation of flow boiling heat transfer coefficient in enhanced tubes. Benchmark correlations and ANN approach, J. Phys. Conf. Ser. 2940 (2025) 012030, https://doi.org/10.1088/1742-6596/2940/1/012030.

[54] H. Liu, Z. Wu, C. Yuan, H. Li, H. Li, J. Peng, L. Huang, Experimental study of R410A and its low GWP alternative R452B flow boiling in a multiport microchannel tube, Int. J. Heat Mass Transf. 230 (2024) 125732, https://doi.org/10.1016/j.ijheatmasstransfer.2024.125732.

[55] E.W. Lemmon, M.L. Huber, M.O. McLinden, NIST Standard Reference Database 23: Reference Fluid Thermodynamic and Transport Properties-REFPROP, Version 9.1, 2013. https://www.nist.gov/publications/nist-standard-reference-database-23-reference-fluid-thermodynamic-and-transport (Accessed 24 April 2022).

[56] B.N. Taylor, C.E. Kuyatt, et al., Guidelines For Evaluating and Expressing the Uncertainty of NIST Measurement Results, US Department of Commerce, Technology Administration, National Institute of Science and Technology, 1994.

[57] S.W. Churchill, R. Usagi, A general expression for the correlation of rates of transfer and other phenomena, AIChE J. 18 (1972) 1121–1128, https://doi.org/10.1002/aic.690180606.

[58] W.W. Akers, H.A. Deans, O.K. Crosser, Condensing heat transfer within horizontal tubes, Chem. Eng. Progr. 55 (29) (1959). Symposium Ser. No. https://www.osti.gov/biblio/4193612 (Accessed 29 September 2022)

[59] W. Qu, I. Mudawar, Measurement and prediction of pressure drop in two-phase micro-channel heat sinks, Int. J. Heat Mass Transf. 46 (2003) 2737–2753, https://doi.org/10.1016/S0017-9310(03)00044-9.

[60] D.F. Sempértegui-Tapia, G. Ribatski, Two-phase frictional pressure drop in horizontal micro-scale channels: experimental data analysis and prediction method development, Int. J. Refrig. 79 (2017) 143–163, https://doi.org/10.1016/j.ijrefrig.2017.03.024.

[61] C.A. Monroe, T.A. Newell, J.C. Chato, An Experimental Investigation of Pressure Drop and Heat Transfer in Internally Enhanced Aluminum Microchannels, Air Conditioning and Refrigeration Center. College of Engineering. University of Illinois at Urbana-Champaign., 2003. https://hdl.handle.net/2142/12167. accessed October 9, 2025.

[62] M. Ducoulombier, S. Colasson, J. Bonjour, P. Haberschill, Carbon dioxide flow boiling in a single microchannel – Part II: heat transfer, Exp. Therm. Fluid Sci. 35 (2011) 597–611, https://doi.org/10.1016/j.expthermflusci.2010.11.014.

[63] R. Yun, J. Hyeok Heo, Y. Kim, Evaporative heat transfer and pressure drop of R410A in microchannels, Int. J. Refrig. 29 (2006) 92–100, https://doi.org/10.1016/j.ijrefrig.2005.08.005.

[64] Y.J. Chang, S.K. Chiang, Two-Phase Frictional Characteristics of R410A and Air-Water in a 5-mm Smooth Tube, 2000, pp. 792–797. https://iifiir.org/en/fridoc/two-phase-frictional-characteristics-of-r410a-and-air-water-in-a-5-mm-18754 (Accessed 6 November 2025).

[65] C.B. Tibiriçá, G. Ribatski, Two-Phase Frictional Pressure Drop and Flow Boiling Heat Transfer for R245fa in a 2.32-mm Tube, Heat Transf. Eng. 32 (2011) 1139–1149, https://doi.org/10.1080/01457632.2011.562725.

[66] R. Revellin, J.R. Thome, Experimental investigation of R-134a and R-245fa two-phase flow in microchannels for different flow conditions, Int. J. Heat Fluid Flow 28 (2007) 63–71, https://doi.org/10.1016/j.ijheatfluidflow.2006.05.009.